Predicting thermal performance of an enhanced geothermal system from tracer tests in a data assimilation framework

Hui Wu[1], Pengcheng Fu[1], Adam J. Hawkins[2], Hewei Tang[1], Joseph P. Morris[1]

[1]Atmospheric, Earth, and Energy Division, Lawrence Livermore National Laboratory, Livermore, CA, USA.

[2]Robert Fredrick Smith School of Chemical and Biomolecular Engineering, Cornell University, Ithaca, NY, USA.

Corresponding author: Hui Wu (wu40@llnl.gov)

Key Points:

- Proposed a data assimilation framework to predict thermal performance of enhanced geothermal system (EGS) from tracer data.
- Demonstrated the efficacy of the framework through a synthetic field-scale EGS model and a meso-scale field test.
- Combining conservative and sorptive tracer data offers more accurate prediction of thermal performance than individual tracer.

Abstract

Predicting the thermal performance of an enhanced geothermal system (EGS) requires a comprehensive characterization of the underlying fracture flow patterns from practically available data such as tracer data. However, due to the inherent complexities of subsurface fractures and the generally insufficient geological/geophysical data, interpreting tracer data for fracture flow characterization and thermal prediction remains a challenging task. The present study aims to tackle the challenge by leveraging a data assimilation method to maximize the utilization of information inherently contained in tracer data, and meanwhile maintain the flexibility to handle various uncertainties. A tracer data interpretation framework was proposed with the following three components integrated: 1) We use principal component analysis (PCA) to reduce the dimensionality of model parameter space. 2) We use ES-MDA (ensemble smoother with multiple data assimilation) to invert for fracture aperture/flow fields and obtain posterior model ensembles for uncertainty quantification. Various data types are assimilated jointly to improve the predictive ability of the posterior ensemble. 3) The inverted fracture aperture fields are then incorporated into reservoir models to predict thermal performance. We developed a field-scale EGS model to verify the ability of the framework to characterize highly heterogeneous fracture aperture/flow fields and predicting thermal performance. We also applied the framework to a meso-scale field experiment to demonstrate its potential application in real-world geothermal reservoirs. The results indicate that the proposed framework can effectively retrieve fracture flow information from tracer data for thermal prediction and uncertainty quantification, and thus provide informative guidance for EGS optimization and risk management.

1 Introduction

A wider deployment of geothermal energy, particularly enhanced geothermal systems (EGS), is considered an essential component of the global effort to combat climate change and environment pollution. The optimization and risk management of EGS require accurate predictions of long-term thermal performance under different stimulation and operation scenarios. As EGS relies on natural and/or artificial fractures for fluid circulation and heat extraction, its thermal performance highly depends on fracture flow characteristics (Fox et al., 2015; Fu et al., 2016; Guo et al., 2016b; Chen and Zhao, 2020). Direct observations and measurements of fractures in an EGS setting that is generally several kilometers below the ground surface are extremely difficult. Remarkable effort has been devoted to investigating indirect hydraulic and geophysical testing methods, such as hydraulic and tracer testing, seismic and electrical methods, ground penetrating radar, etc. (Berkowitz, 2002; Neuman, 2005; Maxwell et al., 2010; Wu et al., 2019). Among these methods, tracer testing is a powerful and widely used approach for subsurface fracture characterization (Sanjuan et al., 2006; Brown et al., 2012; Juliusson and Horne, 2013; Hawkins et al., 2018). By injecting tracer-carrying fluid into one or more target fractures and monitoring tracer concentrations at outlet wells, one can obtain tracer breakthrough curves which are expected to reflect fracture flow characteristics.

Interpreting tracer data for fracture flow characterization and thermal performance prediction of an EGS is challenging. Some methods have been developed to directly predict hydrothermal systems' thermal performance from tracer data, but those are inapplicable to EGS due to a significant difference between the two types of geothermal systems. For hydrothermal reservoirs, the porous medium serves as the reservoir for both the fluid mass ("hydro reservoir")

and heat ("thermal reservoir"). For an EGS, the hydro reservoir is mainly the fracture apertures whereas the thermal reservoir is the rock body surrounding the fractures. This discrepancy makes directly connecting tracer data to thermal performance extremely challenging. Shook (2001) developed a transformation method to derive a thermal breakthrough curve from a tracer breakthrough curve by utilizing the analogies between governing equations for tracer and heat transport, but the method is only applicable to hydrothermal reservoirs. Guo et al. (2016a) attempted to correlate the metrics of tracer breakthrough curves, including peak concentration and mean residence time, to the life span of an EGS, but the obtained correlations were poor. Traditional temporal moment analysis on tracer breakthrough curves can estimate important fracture characteristics such as fracture volume swept by tracer (Shook, 2003; Wu et al., 2008; Ayling et al., 2016; Hawkins et al., 2017b; Tian et al., 2016; Kittilä et al., 2019). However, fracture volume alone is unable to predict EGS thermal performance because heat extraction from an EGS depends largely on the effective heat exchange area, which cannot be directly calculated through conventional tracer test analysis.

A promising strategy is to use inversion-based tracer data interpretation to first characterize fracture aperture/flow fields and then predict EGS thermal performance based on the inversion results. A practical challenge for such inversion problems is that available geological and geophysical data are generally insufficient for constraining the many inherent complexities of subsurface fractures. Some previous studies assumed simplistic fracture models (e.g., homogeneous fracture aperture, fixed shape) to circumvent these complexities, and used analytical solutions to invert for key parameters such as aperture and heat exchange area (Radilla et al., 2012; Shook and Suzuki, 2017; Hawkins et al., 2018; Suzuki et al., 2019). Such simplified approaches, while efficient and easy to implement, may not be able to capture the complex fracture features necessary for thermal prediction, such as highly heterogeneous aperture distribution. An alternative is to develop a fracture model that properly accounts for the complexities and then use high-fidelity numerical simulations for tracer data inversion. The high-dimensional parameter space of the complex fracture model inevitably leads to an ill-posed inversion problem. Inversion approaches that can handle the equifinality of such problems are therefore desired to find multiple viable realizations to quantify uncertainties in thermal prediction. Commonly used approaches include stochastic modeling (Vogt et al., 2012a; Wu et al., 2021), Markov Chain Monte Carlo (MCMC) (Irving and Singha, 2010; Cui et al., 2011; Vrugt, 2016; Zhang et al., 2018) and ensemble-based data assimilation (Evensen, 1994, 2018; van Leeuwen and Evensen, 1996; Chen and Oliver, 2012; Emerick and Reynolds, 2013; Tang et al., 2021). Compared with stochastic modeling and MCMC, ensemble-based data assimilation is computationally more efficient, and has gained increasing popularity in tracer data interpretation for subsurface characterization (Vogt et al., 2012b; Chen et al., 2013; Crestani et al., 2013; Keller et al., 2018). The result of ensemble-based data assimilation is an ensemble of viable model realizations, each of which can reasonably fit tracer data. The variability among these model realizations represents uncertainties arising from different sources.

While important progresses have been made regarding the inversion of aperture/permeability fields from tracer data (Vogt et al., 2012b; Wu et al., 2020; Hawkins et al., 2020), the ability of the inversion results to predict thermal performance requires further investigation. Most of the abovementioned studies focused on aperture/permeability inversion, and only a few discussed the prediction of thermal performance. Vogt et al. (2012b) used an Ensemble Kalman Filter (EnKF) to assimilate conservative tracer data at the Soultz-sous-Forêts EGS reservoir and predicted the thermal performance of the reservoir for 50 years through the

inverted reservoir permeability. However, the predictions showed significant uncertainties. Wu et al. (2020) used a stochastic modeling approach to interpreting a conservative tracer test at the EGS Collab field experiment and inferred spatial aperture distribution in a major hydraulic fracture. Multiple satisfactory aperture distributions were obtained, and the predicted thermal responses from these aperture distributions showed considerable uncertainties.

In the present study, we propose a tracer data interpretation framework to first invert for spatial distribution of fracture aperture, and then predict thermal performance based on the inversion results. Ensemble smoother with multiple data assimilation (ES-MDA) is employed for tracer data interpretation. We aim to 1) Investigate the efficacy of ensemble-based data assimilation in fracture aperture/permeability inversion from tracer data; 2) Examine the suitability of the inversion results for thermal performance prediction; 3) Explore methods (such as joint data assimilation) to improve prediction accuracy and constrain prediction uncertainties. The novelty of the framework includes the following: 1) While most previous studies only assimilate a single type of data (mainly conservative tracer data as abovementioned), the framework employed here jointly assimilates multiple data types, including conservative and sorptive tracer data, as well as practically available pressure and flow data. The effects of combining different data types are analyzed to provide practical guidance for fracture characterization. 3) The framework integrates fracture aperture inversion with reservoir simulation to allow further investigation of the use of inversion results in thermal performance prediction.

The paper is organized as follows. Section 2 describes the main components of the proposed framework. In Section 3, we introduce a synthetic field-scale EGS model to verify the effectiveness of the framework in fracture aperture inversion and thermal performance prediction. Section 4 validates the proposed framework against a meso-scale field experiment at the Altona Field Laboratory (AFL) which involved various tracer tests and a water circulation test. Section 5 provides discussions regarding the capability and limitation of the framework.

2 Tracer data interpretation framework

There are three major components in the proposed framework (Fig. 1): 1) Model parameterization and dimensionality reduction; 2) ES-MDA to invert for fracture characteristics

from tracer data; and 3) Thermal performance prediction based on the inversion results from ES-MDA. Sections 2.1 to 2.3 describe details of these three components, respectively.

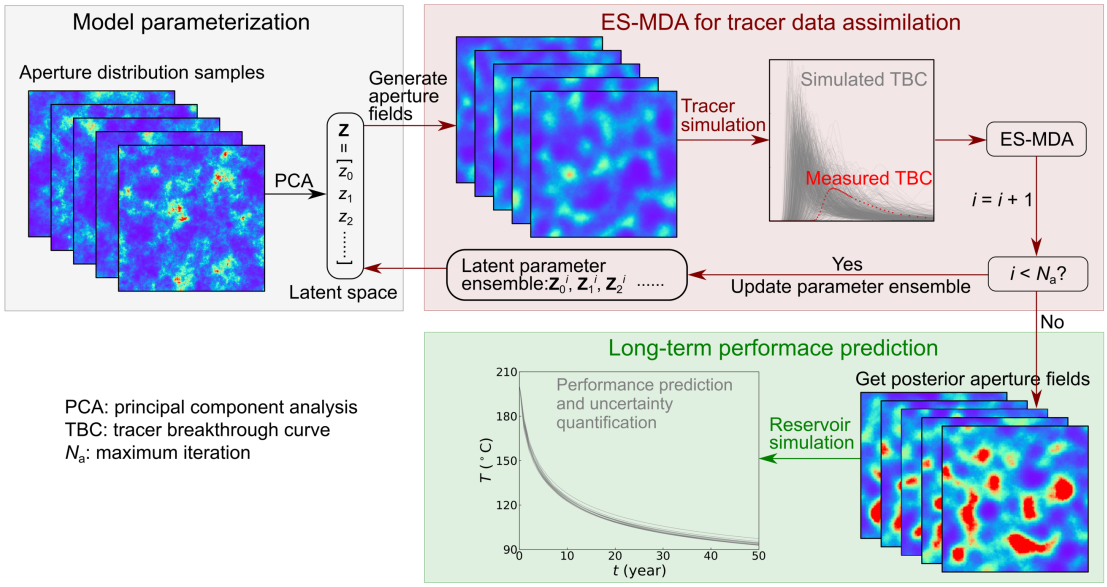

Fig. 1 Workflow of the tracer data interpretation framework. Aperture distribution within a single, discrete fracture is shown as 2D spatially correlated random fields.

2.1 Model parameterization and dimensionality reduction

Driven by data scarcity in subsurface characterization problems, we need to parameterize reservoir models with an appropriate level of complexity. The concerned parameter in the present study is the spatial distribution of aperture in a discrete rock fracture, which is usually described by 2D spatially correlated fields (Fig. 1). In real-world problems, fracture aperture is generally highly heterogeneous following Gaussian (Pyrak-Nolte and Morris, 2000; Guo et al., 2016a; Wu et al., 2021) or non-Gaussian distributions (Power and Tullis, 1992). Cell-based parameterization of aperture fields results in a large parameter space, and the auto-correlation of aperture is not naturally honored. To address this issue, the proposed framework employs principal component analysis (PCA) to reduce the dimensionality of the parameter space.

PCA is a widely used unsupervised technique to project high-dimensional data to a latent space defined by orthogonal principal components. These principal components can be obtained through either computing the eigenvectors and eigenvalues of the covariance matrix of the original high-dimensional data or directly performing singular value decomposition (SVD) on the original data. The principal components are then ordered in such a way that the higher-ranked principal components preserve greater variance in the original data. By truncating the vector of principal components, the original data can be represented by a low-dimensional latent space while preserving most of the variance or "energy" in the original data. PCA has been widely used to reduce the dimensionality of spatially correlated fields, such as permeability and aperture distribution, in history matching and inversion problems pertaining to subsurface aquifer/reservoir characterization (Sarma et al., 2008; Hawkins et al., 2020). Below we briefly introduce the major steps of PCA through SVD (Liu and Durlofsky, 2020).

- Prior to PCA, we first generate an ensemble of aperture fields (cell-based values) according to our prior knowledge from geological/geophysical measurements,

such as core logs, wellbore images and outcrop analysis. The generated sample fields, denoted as $\mathbf{M} = [\mathbf{m}_1\ \mathbf{m}_2\ \ldots\ \mathbf{m}_{N_r}] \in \mathbb{R}^{N_c \times N_r}$, where N_c is the number of unknows (i.e., the number of discretized cells) in each sample field and N_r is the number of generated sample fields, are provided to PCA as training data. The N_r fields collectively represent the range of variations of the aperture field.

- The sample fields are assembled into a matrix $\mathbf{M}_c$ as,

$$\mathbf{M}_c = \frac{1}{\sqrt{N_r - 1}}\left[\mathbf{m}_1 - \bar{\mathbf{m}}\ \ \mathbf{m}_2 - \bar{\mathbf{m}}\ \ \ldots\ \mathbf{m}_{N_r} - \bar{\mathbf{m}}\right] \quad (1)$$

where $\bar{\mathbf{m}}$ denotes the mean of the N_r sample fields.

- SVD is then performed on $\mathbf{M}_c$ to obtain singular values and matrices,

$$\mathbf{M}_c = \mathbf{U}\boldsymbol{\Sigma}\mathbf{V}^T \quad (2)$$

where $\mathbf{U} \in \mathbb{R}^{N_c \times N_r}$ and $\mathbf{V} \in \mathbb{R}^{N_r \times N_r}$ are the left and right singular matrices, respectively, and $\boldsymbol{\Sigma} \in \mathbb{R}^{N_r \times N_r}$ is a diagonal matrix with each diagonal element as a singular value.

- We then select sub-matrices $\mathbf{U}_l$ and $\boldsymbol{\Sigma}_l$, where $\mathbf{U}_l \in \mathbb{R}^{N_c \times l}$ contains the first l ($l \ll N_c$) columns in $\mathbf{U}$ and $\boldsymbol{\Sigma}_l \in \mathbb{R}^{l \times l}$ is a diagonal matrix containing the first l singular values in $\boldsymbol{\Sigma}$. An original sample field $\mathbf{m}_i$ can be reconstructed from a latent parameter vector $\mathbf{z}_i$ using the following equations,

$$\mathbf{z}_i = \boldsymbol{\Sigma}_l^{-1}\mathbf{U}_l^T(\mathbf{m}_i - \bar{\mathbf{m}}) \quad (3)$$

$$\hat{\mathbf{m}}_i = \bar{\mathbf{m}} + \mathbf{U}_l\boldsymbol{\Sigma}_l\mathbf{z}_i \quad (4)$$

where $\hat{\mathbf{m}}_i$ is the reconstructed sample field for $\mathbf{m}_i$.

- New sample fields can also be generated from,

$$\mathbf{m}(\mathbf{z}) = \bar{\mathbf{m}} + \mathbf{U}_l\boldsymbol{\Sigma}_l\mathbf{z} \quad (5)$$

where $\boldsymbol{z}$ is a l-dimensional latent parameter vector with each element independently sampled from the standard normal distribution.

After dimensionality reduction using PCA, the high-dimensional aperture field $\mathbf{m}$ can be represented by a low-dimensional latent space $\mathbf{z}$. In section 3.3, we demonstrate the reconstruction of an original aperture field from latent space, and also analyze the effect of the dimensionality of $\mathbf{z}$.

2.2 ES-MDA for tracer data interpretation

The second step in the proposed framework is to invert for latent parameters by assimilating tracer data using ES-MDA. ES-MDA, developed by Emerick and Reynolds (2013), uses an iterative scheme to assimilate historical data multiple times and update model parameters so that model responses match the historical data to a satisfactory level. Compared with other ensemble-based data assimilation methods such as EnKF and Ensemble Smoother (ES), ES-MDA alleviates the computational burden of EnKF by assimilating all historical data simultaneously and addresses the unsatisfactory data matching quality in ES by assimilating the historical data multiple times. The detailed derivation of ES-MDA is described in Emerick and Reynolds (2013), and below we briefly introduce the main procedures of ES-MDA for tracer data interpretation (Fig. 1).

- First, a prior ensemble of parameter sets is generated according to the prior distribution of model parameters. In the proposed framework, the prior ensemble of latent parameters, denoted as $\mathbf{Z}^0 = [\mathbf{z}_1^0\ \mathbf{z}_2^0\ \dots\ \mathbf{z}_{N_e}^0] \in \mathbb{R}^{l \times N_e}$ where N_e is the number of parameter sets (ensemble size), can be generated by randomly sampling from the standard normal distribution.
- With the prior ensemble, we can generate the corresponding aperture fields through equation (5), denoted as $\mathbf{M}^0 = [\mathbf{m}(\mathbf{z}_1^0)\ \mathbf{m}(\mathbf{z}_2^0)\ \dots\ \mathbf{m}(\mathbf{z}_{N_e}^0)] \in \mathbb{R}^{N_c \times N_e}$. We then calculate model responses for each aperture field according to forward model $\mathbf{y}_i^0 = f(\mathbf{m}(\mathbf{z}_i^0)) \in \mathbb{R}^{N_d}$, where 0 in the superscript denotes the iteration number. $i = 1, 2, \dots, N_e$, and N_d is the number of measurements. f and $\mathbf{y}$ denote the forward model and the corresponding model response, respectively. For the analysis of tracer data, f is a tracer simulation model and $\mathbf{y}$ is tracer breakthrough data.
- The following equation is then used to update the prior ensemble iteratively,

$$\mathbf{z}_i^n = \mathbf{z}_i^{n-1} + \mathbf{C}_{ZY}^{n-1}(\mathbf{C}_{YY}^{n-1} + \alpha_n \mathbf{C}_Y^{n-1})^{-1}(\mathbf{y}_{obs} + \boldsymbol{\epsilon}_i - \mathbf{y}_i^{n-1}) \quad (6)$$

where $n = 1, 2, \dots, N_a$, denoting the iteration of ES-MDA. N_a is the user-defined data assimilation number. $\mathbf{z}_i^n$ is the updated parameter sets after the current iteration. $\mathbf{C}_{ZY} \in \mathbb{R}^{l \times N_d}$ is the cross-covariance matrix between the current parameter ensemble $\mathbf{Z}^{n-1} = [\mathbf{z}_1^{n-1}\ \mathbf{z}_2^{n-1}\ \dots\ \mathbf{z}_{N_e}^{n-1}] \in \mathbb{R}^{l \times N_e}$ and the corresponding model responses $\mathbf{y}^{n-1} = [\mathbf{y}_1^{n-1}\ \mathbf{y}_2^{n-1}\ \dots\ \mathbf{y}_{N_e}^{n-1}] \in \mathbb{R}^{N_d \times N_e}$. $\mathbf{C}_{YY} \in \mathbb{R}^{N_d \times N_d}$ is the auto-covariance matrix of model responses. $\mathbf{C}_Y \in \mathbb{R}^{N_d \times N_d}$ is the covariance matrix of the measurement errors of the historical data being assimilated, i.e., $\mathbf{y}_{obs}$. $\boldsymbol{\epsilon}_i$ is random Gaussian noise drawn from $N(0, \alpha_n \mathbf{C}_Y)$. α_n is the user-defined inflation coefficient at the current iteration. According to Emerick and Reynolds (2013), the following condition should be satisfied,

$$\sum_{n=1}^{N_a} \frac{1}{\alpha^n} = 1 \quad (7)$$

After N_a updates, we can obtain the posterior ensemble of parameter sets $\mathbf{Z}^{N_a}$ as well as the corresponding posterior aperture distributions.

2.3 Thermal performance prediction

Another major component of the proposed framework is a thermal performance prediction module using the obtained posterior ensemble of aperture distributions. We incorporate the posterior aperture distributions into 3D reservoir models and perform simulations to predict long-term thermal performance. The predictions from different aperture distributions in the posterior ensemble represent the prediction uncertainty.

3 Demonstration using a field-scale single-fracture EGS model

In this section, we develop a field-scale EGS model to generate synthetic data to evaluate the effectiveness of the proposed framework in predicting thermal performance. The EGS model involves a dominant horizontal fracture in a large body of low permeability crystalline rock. An injection well and two production wells are drilled into the rock formation and intersect the fracture (Fig. 2). The application of the proposed framework to EGS consisting of multiple or many fractures will be addressed in future work. We perform tracer and thermal simulations to obtain synthetic tracer, pressure, and flow rate data as well as thermal breakthrough curves at the

two production wells. The framework in Fig. 1 is then used to predict the thermal breakthrough curves from the tracer, pressure and flow rate data.

3.1 Model setup

The dimensions of the EGS model are 3000 × 3000 × 3000 m^3 (Fig. 2). The horizontal fracture is located in the center of the model with a size of 800 × 800 m^2. The square shape of the hypothetical fracture was for convenience. The somewhat unrealistic and idealized geometric shape still fulfills the needs for generating synthetic data and validate the workflow. A vertical temperature gradient of 40 °C/km is assumed in the model with an initial temperature of 140 °C at model top. The temperature at the fracture depth is therefore 200 °C. The fracture is represented by a thin layer of elements 5 × 5 × 0.004 m^3 in size. The mesh resolution of the rock matrix is 5 × 5 × 2.5 m^3 near the fracture and becomes progressively coarser in the far field. The resulting computational domain consists of approximately 2,800,000 elements.

To demonstrate the efficacy of the proposed framework, we desire the fracture's aperture to be highly heterogeneous (Fig. 2). We use the following procedure to generate the aperture distribution: 1) We first generate a random 160 × 160 gaussian field and then transform the gaussian field to a binary facies field: Voxel values smaller than a threshold are reassigned as zero and the others as one. 2) Each facies in the binary field is populated with an independently generated random gaussian fields following a log-normal distribution. The "background" facies, visible as the green-to-red area in Fig. 2 has a mean aperture of 3 mm, a standard deviation of 2 mm, and a correlation length of 300 m. The "inclusion" facies, visible as the blue patches, has a mean aperture of 0.6 mm, a standard deviation of 0.4 mm and a correlation length of 500 m.

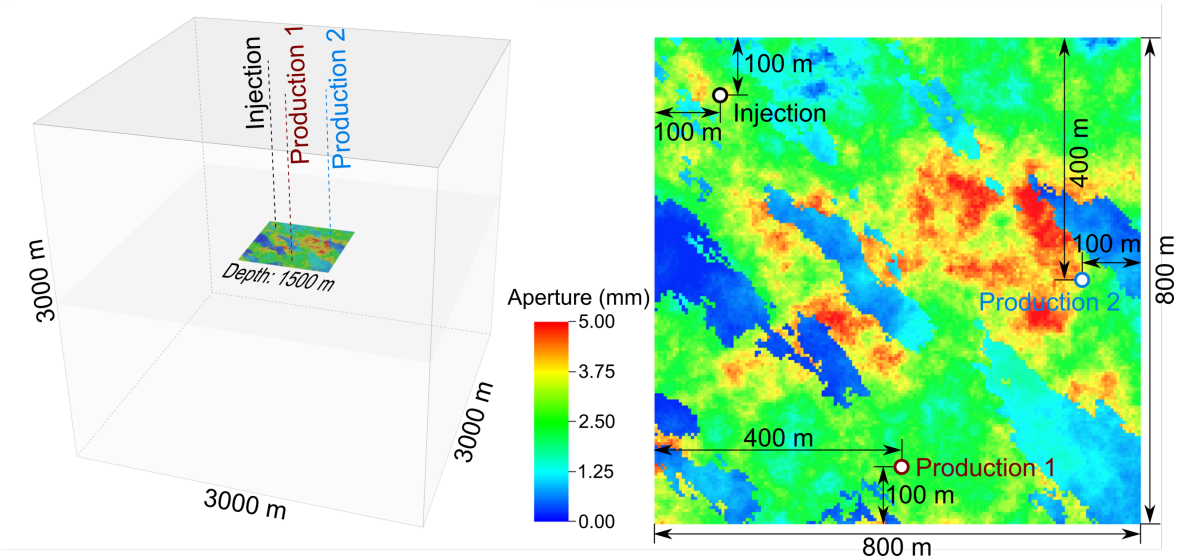

Fig. 2 A field-scale EGS model with a horizontal fracture connecting an injection and two production wells. Left: Spatial relationship between the simulation domain, the fracture, and the three wells. Right: The spatial distribution of fracture aperture in a plan view.

3.2 Tracer and thermal modeling

We use GEOS, a massively parallel multi-physics simulation platform developed at the Lawrence Livermore National Laboratory (Settgast et al., 2017), for tracer and thermal modeling

in the present study. The tracer transport module in GEOS has been detailed in Guo et al. (2016a) and Wu et al. (2021), and readers are referred to Guo et al. (2016b) for the details of the thermal module in GEOS.

For tracer modeling, we include both conservative and sorptive tracers. A hydrostatic initial pressure is assumed in the model with a pressure of 30 MPa at the fracture depth. The injection rate is 10 L/s and we keep constant downhole pressure (30 MPa) at the two production wells. Tracers are injected into the horizontal fracture for one hour and we simulate the tracer transport process for 40 hours to obtain tracer breakthrough curves at the two production wells. Because the fracture is represented by a thin layer of porous media, we calculate the equivalent porosity and permeability of the fracture layer through $\phi = w/H$ and $k = w^3/12H$ respectively (Guo et al., 2016a), where w is the aperture and $H = 4$ mm is the thickness of the fracture grid elements. Other parameters for tracer modeling are listed in Table 1. For sorptive tracer modeling, we assume an equilibrium sorption process with a partition coefficient of 0.3 mm. For a typical matrix diffusion coefficient of 1×10^{-9} m^2/s, we found that the rock formation surrounding the fracture has little effect on the tracer transport process in the fracture. Therefore, we assume that tracer transport is confined to the target fracture and only the horizontal fracture is considered for tracer modeling. Fracture boundaries are assumed impermeable.

The simulated tracer breakthrough curves at the two production wells are shown in Fig. 3(a). Due to sorption, the breakthrough curves for the sorptive tracer have delayed peaks with smaller peak magnitudes compared with the counterparts for conservative tracer. The simulated pressure difference between the injection and production wells is 2.8 kPa, and the simulated production rates at production wells 1 and 2 are 2.84 and 7.16 L/s respectively. For both conservative and sorptive tracers, tracer breakthrough is earlier and peak magnitude is smaller at production well 1 than at production well 2.

For thermal modeling, we circulate water among the injection and production wells with an injection rate of 20 L/s and an injection temperature of 50 °C for 50 years. Similar to tracer modeling, we keep the downhole pressure at 30 MPa at the two production wells. The upper, lower and lateral model boundaries are assumed impermeable to both fluid and heat. This is justified because 1) the rock matrix is largely impermeable, and 2) the cooling front at the end of 50 years is still far from the boundary. Parameters for thermal modeling are also summarized in Table 1. We assume constant water viscosity independent of temperature. We do not consider thermo-mechanical coupling in the thermal modeling. As shown in Fig. 3(b), the temperature decrease at production well 1 is slower than that at production well 2 due to the relatively smaller production rate.

The tracer breakthrough curves in Fig. 3(a) as well as the pressure and flow rate data are then used as synthetic "measurements" for subsequent ES-MDA to invert for the aperture distribution in the fracture. The goal is to predict the flow rate-averaged production temperature curve in Fig. 3(b) from the posterior aperture distributions obtained from ES-MDA.

Table 1 Parameters for tracer and thermal modeling of the field-scale EGS model.

Parameter	Value
Porosity of rock matrix	0.01
Permeability of rock matrix (m^2)	1×10^{-16}
Density of rock matrix (kg/m^3)	2500
Specific heat capacity of rock matrix (J/kg/K)	790
Thermal conductivity of rock matrix (W/m/K)	2.5
Density of water (kg/m^3)	887.2
Dynamic viscosity of water (Pa·s)	1.42×10^{-4}
Compressibility of water (Pa^{-1})	5×10^{-10}
Specific heat capacity of water (J/kg/K)	4460
Longitudinal dispersivity (m)	0.2
Transverse dispersivity (m)	0.02
Partition coefficient (mm)	0.3

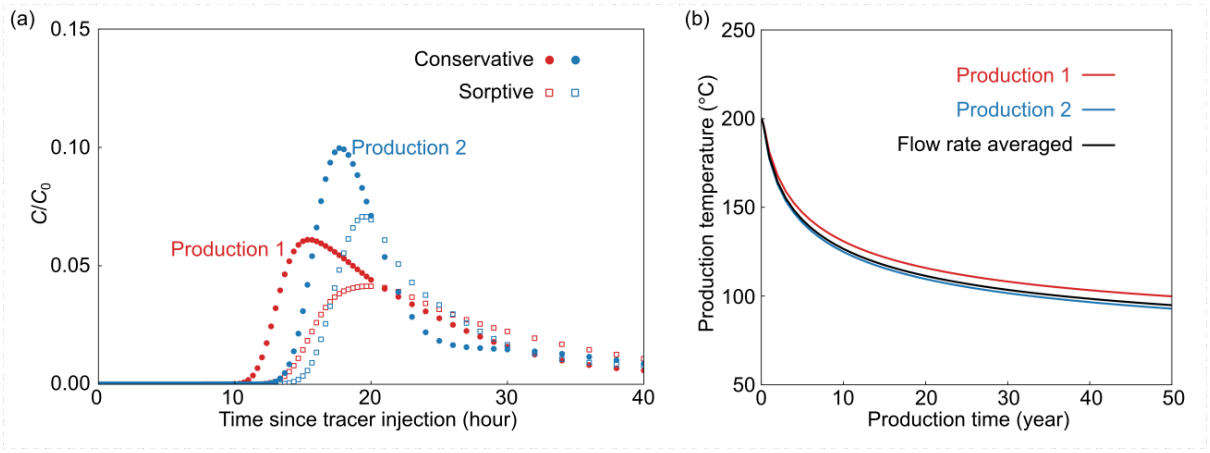

Fig. 3 Tracer and thermal modeling results for the synthetic field-scale EGS model. (a) Tracer breakthrough curves at the two production wells. The monitored tracer concentration is normalized by injection concentration C_0. (b) Thermal breakthrough curves at the two production wells. The black curve is flow rate-averaged production temperature.

3.3 Dimensionality reduction of the aperture field

In real-world applications, fracture aperture distributions are not known *a priori*. To represent inevitable biases in aperture distribution characterization, we intentionally assume a

log-normal aperture distribution for subsequent ES-MDA in this case study. Note that the "ground truth" aperture field in Fig. 2 does not follow a log-normal distribution.

We use sequential gaussian simulations to generate N_r = 5,000 spatially correlated aperture fields from a spherical variogram with a mean of 1 mm, a standard deviation of 0.83 mm and a correlation length of 100 m. All of the generated aperture fields follow a log-normal distribution. Note that we ignore the anisotropy of the aperture field as seen in Fig. 2, another deliberate erroneous bias introduced to test the robustness of the method. We then perform PCA on these 5,000 sample aperture fields according to the procedures in Section 2.1 to obtain the principal components. The level of details retained (i.e. fidelity) by aperture fields reconstructed from equations (3) and (4) depends on the dimension of the latent space. If the hyper parameter l = 5,000, the original aperture field can be fully reconstructed. With decreasing l, the reconstructed aperture fields appear smoother (Fig. 4). Some fine features are missed in the reconstructed aperture fields, but the major patterns are preserved.

In the following ES-MDA process, we select the first 200 principal components (l = 200) as the basis for new aperture field generation. The goal of ES-MDA is therefore to invert for the 200 latent parameters.

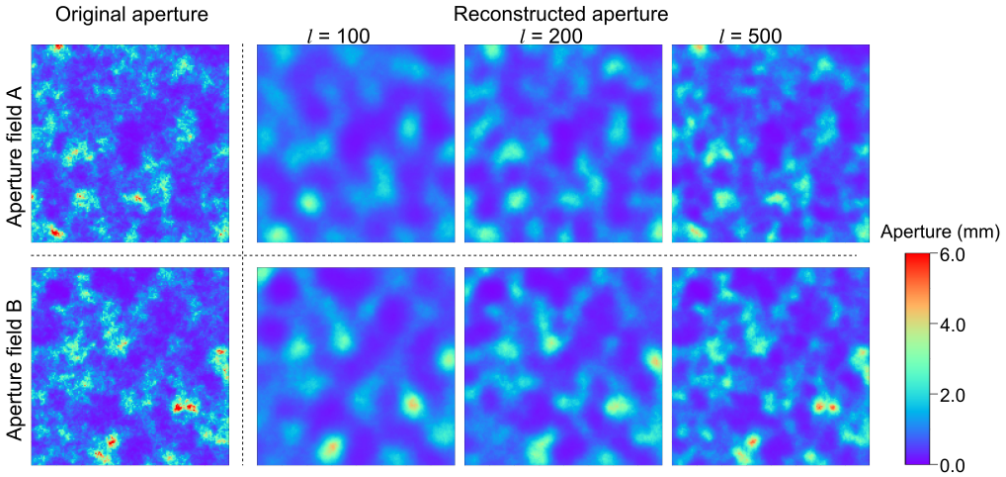

Fig. 4 Reconstruction of two aperture fields with varying numbers of principal components. Approximately 61%, 76% and 86% of the total variance or "energy" in the original aperture fields are preserved with l = 100, 200 and 500 respectively.

3.4 ES-MDA on tracer, pressure and flow rate data

In this section, we use the ES-MDA as laid out in Section 2.2 to assimilate the tracer, pressure and flow rate data in Section 3.2. Each tracer breakthrough curve in Fig. 3(a) contains 105 data points. Together with the pressure difference and the two flow rates, we have 423 data points in total (N_d = 423). We add random gaussian noise to the data, using standard deviations as follows: 1) For the tracer data, the standard deviation is 3% of the peak magnitude in Fig. 3(a). 2) For the pressure and flow rate data, the standard deviation is 1.5% of the observed values. These standard deviations are used to calculate the covariance matrix of the measurement errors $\mathbf{C}_Y$ in equation (6). The total data assimilation number is 12 (N_a = 12). We set gradually decreasing inflation coefficients as suggested by Emerick and Reynolds (2013). After each iteration, we decrease the inflation coefficient by 10%. According to equation (7), the inflation

coefficients for the 12 iterations are 22.9, 20.6, 18.5, 16.7, 15.0, 13.5, 12.2, 10.9, 9.8, 8.8, 7.9, and 7.1 respectively.

We first generate 800 latent parameter sets as the prior ensemble (N_e = 800) by randomly sampling from the standard normal distribution. For each latent parameter set in the prior ensemble, we generate a prior aperture field using the PCA results in Section 3.3 and perform tracer modeling to obtain the prior simulations of tracer, pressure and flow rate (Fig. 5). Afterward, we use equation (6) to update the latent parameter sets for 12 iterations. In each iteration, we repeat the aperture field generation and tracer modeling steps using the updated latent parameter sets. After the last iteration, we obtain posterior latent parameter sets and aperture fields. The tracer breakthrough curves simulated by the posterior aperture fields match the "true" tracer breakthrough curves much better than those predicted by the prior aperture fields (Fig. 5(a)). With the update of the latent parameter sets, the simulated pressure and flow rate also gradually approach to the "true" values (Fig. 5(b)). The differences in posterior simulations among the 800 realizations represent uncertainties from measurement errors (Gaussian noise in this case) and biases in the prior knowledge of the aperture fields.

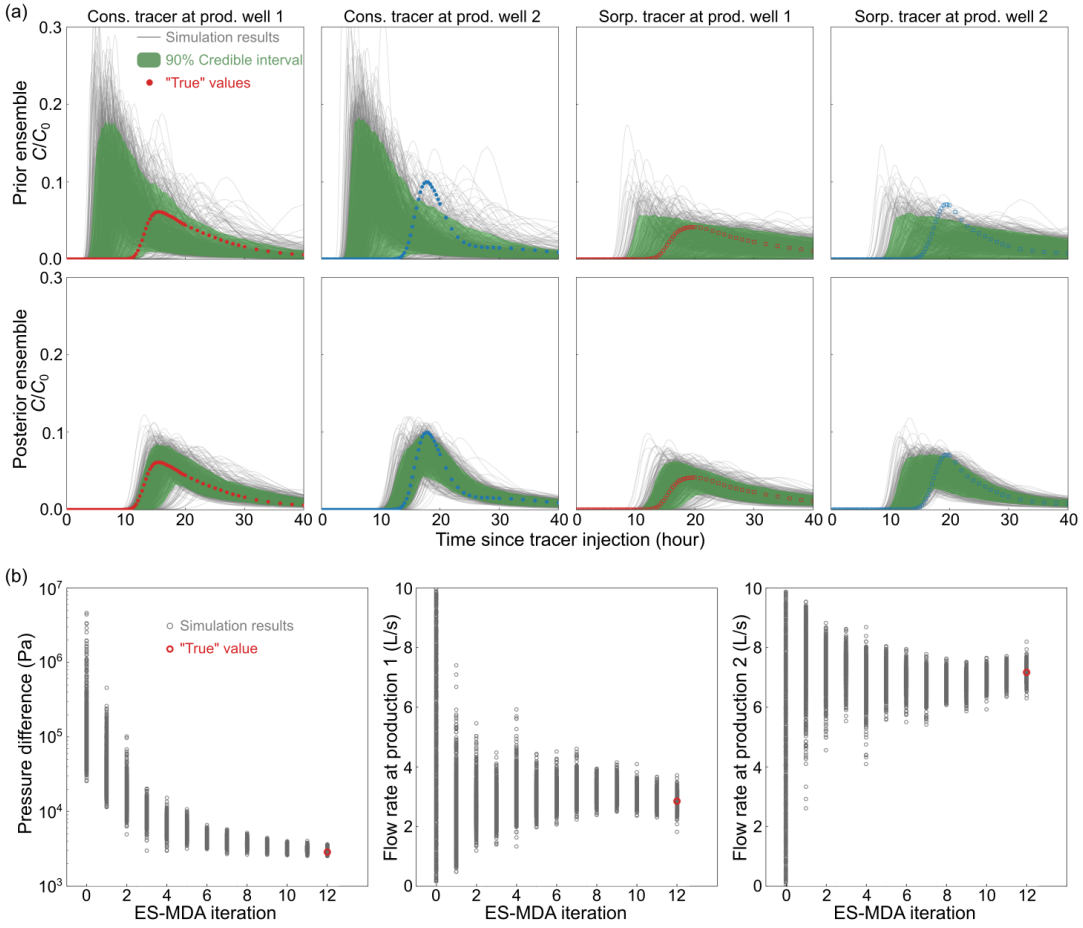

Fig. 5 Simulations of tracer, pressure and flow rate from prior and posterior realizations for the synthetic field-scale model. (a) Comparison between the predicted and "true" tracer breakthrough curves. The upper row shows the comparison for the prior ensemble, and the lower row is the comparison for the posterior ensemble. All the predicted tracer breakthrough curves

from the 800 realizations in the ensemble are shown (grey curves). The green shadings are the 90% credible intervals for the predicted tracer breakthrough curves. (b) The evolution of the predicted pressure and flow rate with respect to ES-MDA iterations. For each iteration, the predicted pressure and flow rate from the 800 realizations are shown (grey circles). The "true" values are annotated by red circles situated along the final iteration.

3.5 Analysis of aperture distribution and fracture flow characteristics

With the posterior ensemble from ES-MDA, we can analyze the spatial distribution of aperture as well as flow characteristics in the fracture to compare with the synthetic "ground truth". We first randomly select an aperture realization from the prior ensemble to compare with the true aperture field. The true flow field (first row in Fig. 6) has two major flow channels connecting the injection well and the two production wells respectively. However, the flow field from the randomly selected prior realization (second row in Fig. 6) exhibits distinct flow patterns with three flow channels connecting the injection and production wells. After 12 ES-MDA iterations, the corresponding posterior realization's flow field (third row in Fig. 6) qualitatively resembles the true flow field. The two major flow channels in the true flow field are approximately resolved.

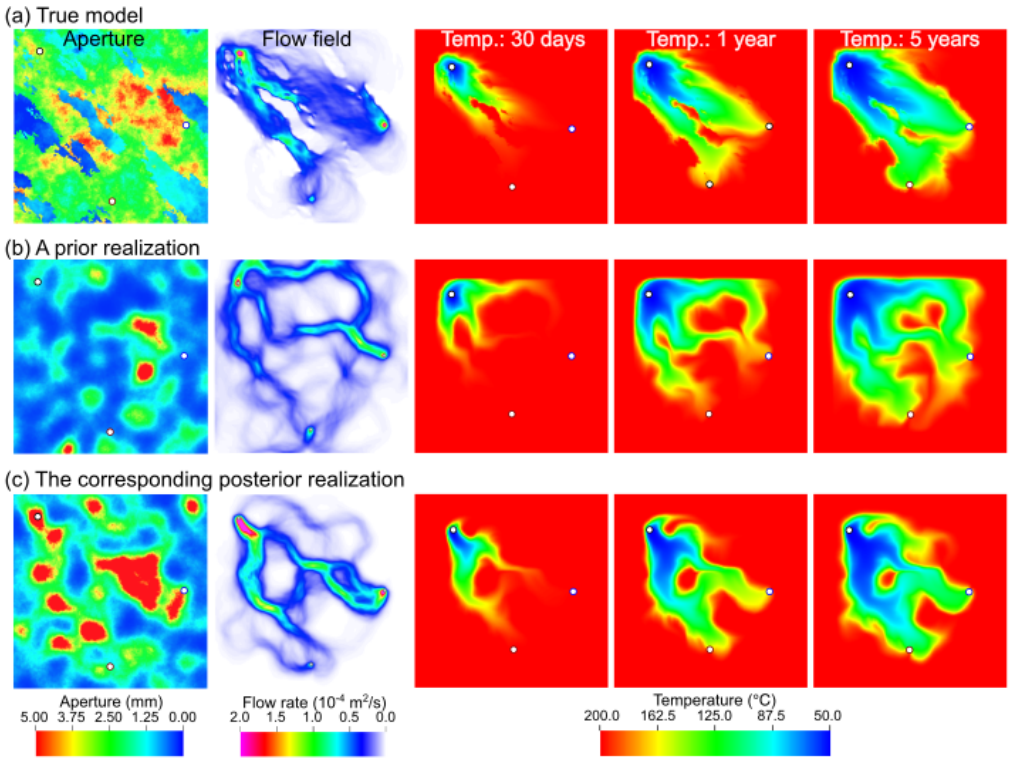

Fig. 6 Comparison of aperture distribution, flow field and temperature (Temp.) evolution in the fracture among (a) the true model, (b) a prior realization randomly selected from the prior ensemble, and (c) the corresponding posterior realization from the posterior ensemble. The flow rate is the volume of water passing a unit-length cross section of the fracture per unit time. Note that we only show the temperature distribution on the fracture plane for clarity.

The average aperture from all 800 realizations is shown in Fig. 7. For the prior ensemble, since each aperture realization is an independently generated random field, the average aperture

is almost uniform. The corresponding average flow field exhibits a relatively homogeneous pattern among the injection and production wells without any remarkable flow channel. The posterior aperture distributions, on the contrary, show significant common patterns among the 800 realizations. The average aperture for the posterior ensemble is far more heterogeneous than that for the prior ensemble. Correspondingly, the average flow field for the posterior ensemble exhibits strong flow channels between the injection and production wells, which are similar to that in the true flow field in Fig. 6.

It is important to note that the posterior ensemble's average aperture field is still quite different from the "ground truth" aperture in Fig. 2. This is not surprising because the true aperture field follows a complex distribution that is not covered by the constructed parameter space for the ensemble. Matching the aperture field is not a goal of our approach. The success of the method is measured by its ability to predict the thermal performance as presented in the next sub-section. As thermal response of the system is directly determined by the flow distribution but only indirectly affected by the aperture distribution, the predicted thermal response could be accurate as long as the flow field is reasonably resolved, even if the underlying aperture field is very different from the ground truth.

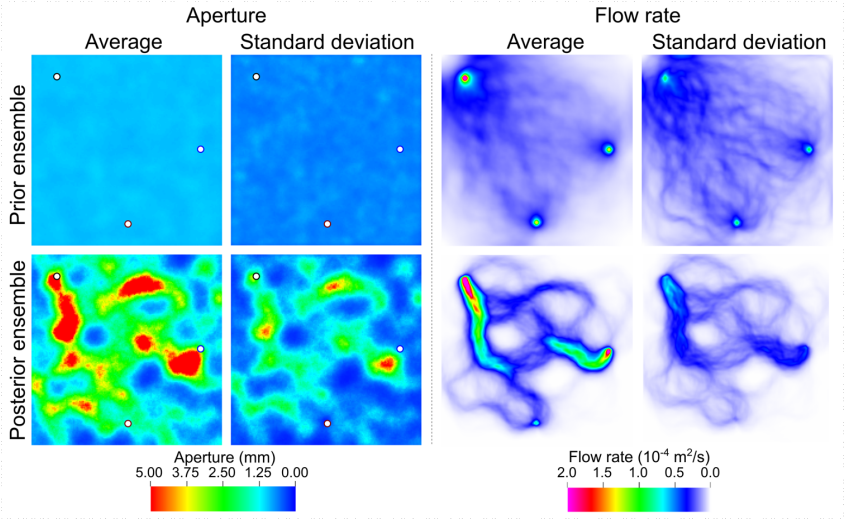

Fig. 7 Average and standard deviation of aperture distribution and flow rate calculated from prior (upper row) and posterior (lower row) ensembles.

3.6 Thermal performance prediction

To investigate the suitability of the posterior ensemble for predicting thermal performance, we perform thermal simulations on both the prior and posterior ensembles. Fig. 8 shows the predicted flow rate-averaged thermal breakthrough curves from these realizations. Results for only 50 randomly selected realizations are shown to avoid over-crowding the visualization. Most of the prior realizations have a slower temperature decrease compared with the true temperature response, and there is a large uncertainty among the predictions from the 50 prior realizations (Fig. 8(a)). This is expected because the prior ensemble was essentially non-calibrated. On the other hand, the predictions from the posterior realizations show a much smaller uncertainty, and the true temperature response is reasonably predicted (Fig. 8(b)). By conditioning the aperture field on tracer, pressure and flow rate data through the proposed framework, we successfully resolve the major flow channels in the true flow field and the

obtained posterior aperture distributions are capable of predicting long-term thermal performance.

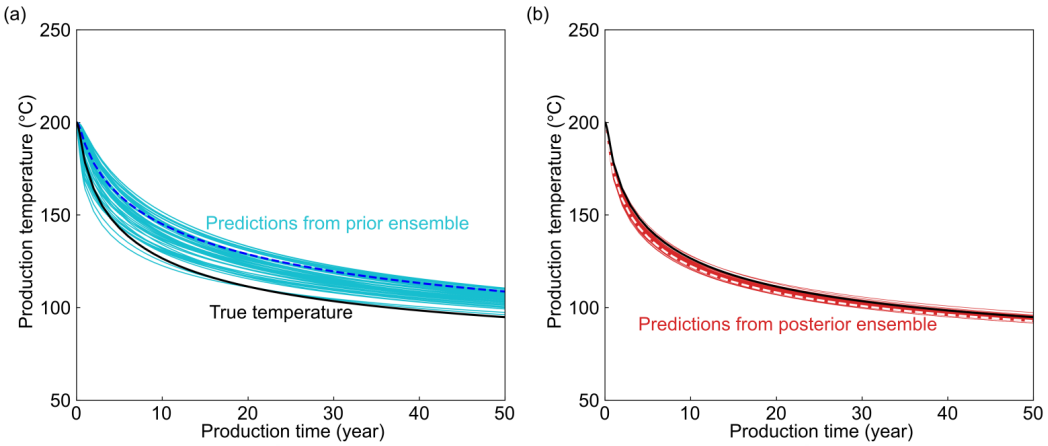

Fig. 8 Prediction of thermal performance (flow rate-averaged thermal breakthrough curve) from the prior (a) and posterior (b) ensembles. The solid black line is the "true" thermal breakthrough curve. The dash blue line (left) and dash white line (right) are the results for the realization visualized in Fig. 6. The cyan (left) and red (right) lines are the results for 50 randomly selected aperture realizations from the prior and posterior ensembles, respectively.

The thermal breakthrough curves corresponding to the prior and posterior realizations in Fig. 6 are also shown in Fig. 8 (dash lines). To understand the greatly improved thermal predictive ability of the posterior realization, the third to fifth columns in Fig. 6 further compare the simulated temperature evolutions in the fracture corresponding to the true aperture field as well as the prior and posterior aperture fields. The temperature distribution in the fracture highly depends on the underlying flow patterns. Because the posterior aperture reasonably resolves the true flow field, the temperature evolution predicted by the posterior aperture is quite accurate.

3.7 Effect of incorporating different data types in data assimilation

In the above analysis, we incorporate all the available data, including conservative and sorptive tracer data, pressure data and flow rate data, in ES-MDA for aperture inference. This section investigates the effects of incorporating different data types by separately assimilating these data with ES-MDA. Four extra ES-MDAs are performed: 1) Conservative tracer data only, 2) conservative tracer data as well as pressure and flow rate data, 3) Sorptive tracer data only, and 4) both conservative and sorptive tracer data, without pressure or flow rates. For each ES-MDA, we use the same procedure as that in Section 3.4 to generate a posterior ensemble, and perform thermal simulations to predict thermal performance (Fig. 9). Compared with the prior predictions in Fig. 8(a), all the posterior predictions in Fig. 9 show a reduced uncertainty. When only conservative tracer data are assimilated, the predicted temperature is systematically higher than the true temperature, indicating systematic biases in the obtained posterior aperture distributions. Note that the prior ensemble has the same bias, namely higher predicted temperature. The bias in the posterior predictions is likely due to the conservative tracer recovery being insensitive to this bias, instead of being introduced by the conservative tracer data itself. Adding pressure and flow rate data to ES-MDA somewhat improves the prediction accuracy, but the results are still poor. Compared with conservative tracer data, sorptive tracer data is more

effective in constraining the prediction of temperature response as demonstrated by the significantly better results in Fig. 9(c) than (a). This is because sorptive tracer data is more sensitive to the interaction area between fracture fluid and surrounding rock formations than conservative tracer, and therefore can better characterize fluid-rock interaction area which is critical for thermal prediction. When conservative and sorptive tracer data are assimilated simultaneously, the temperature response can be accurately predicted. Tracer data, especially sorptive tracer data, are critical for the proposed framework to correctly characterize fracture flow and predict thermal performance.

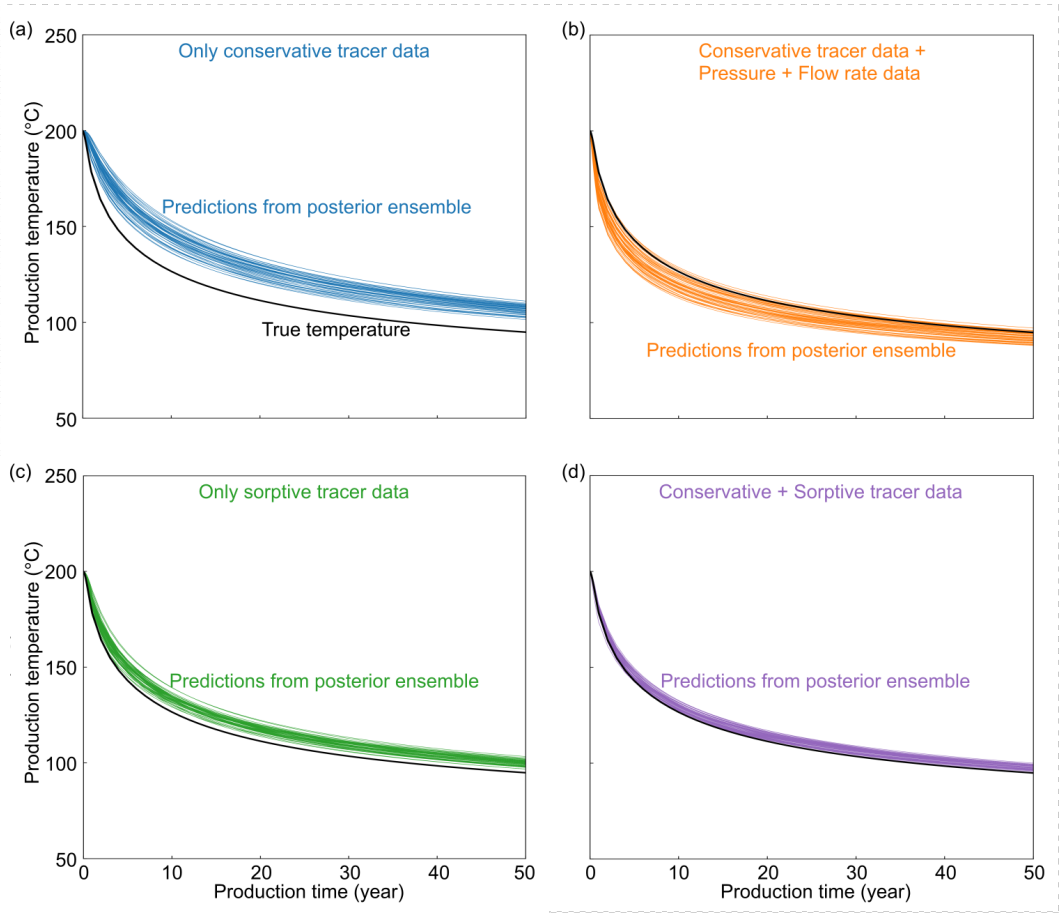

Fig. 9 Prediction of thermal performance (flow rate-averaged thermal breakthrough curve) from posterior ensembles obtained by assimilating different data types. The assimilated data type is annotated in each plot: (a) Conservative tracer data. (b) Conservative tracer data, pressure and flow rate data. (c) Sorptive tracer data. (d) Conservative and sorptive tracer data.

According to the predictions in Figs. 8 and 9, we can estimate the production life span of the field scale EGS model. We use a temperature threshold of 120 °C to determine the "useable" life of an EGS, i.e., the EGS terminates when the production temperature decreases to below 120 °C. Fig. 10 compares the estimated production life spans from the prior ensemble as well as the five posterior ensembles obtained by assimilating different data types. The uncertainty of the production life span (difference between minimum and maximum predictions) is approximately 22 years for the prior ensemble and decreases to less than 4 years for the two posterior ensembles with both conservative and sorptive tracer data assimilated. It is also worth mentioning that the

mean production life span estimated from the two posterior ensembles is very close to the true value.

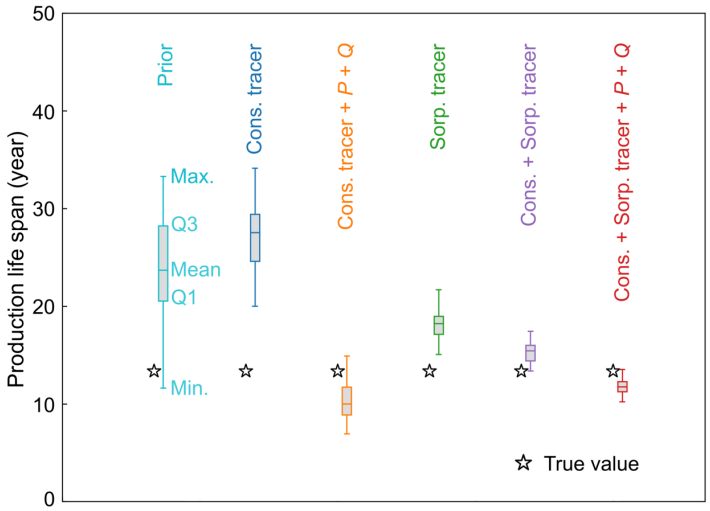

Fig. 10 Production life span estimated from temperature response predictions. The box plots show the minimum, maximum, mean, as well as the 25% (Q1) and 75% (Q3) percentiles. *P* and *Q* represent the pressure and flow rate data respectively.

4 Validation based on a meso-scale field experiment

In this section, we apply the proposed framework to a meso-scale field experiment to further validate its capability in real-world applications. The meso-scale field experiment was performed at the Altona Field Laboratory (AFL) located in the Altona Flat Rocks region in northern New York State, USA (Hawkins et al., 2017a, 2018, 2021). The testbed of the field experiment involves a sub-horizontal fracture approximately 7.6 m below the ground surface. A series of tests were conducted in the testbed to investigate heat and mass transfer processes relevant to geothermal applications, including conservative and sorptive tracer tests as well as a thermal test (Hawkins et al., 2017a, 2018). The obtained tracer and thermal data provide a unique opportunity to validate the proposed framework.

The well configuration and geological condition of the testbed has been reported in the literature (Hawkins et al., 2017a, 2018, 2020) and therefore not repeated here. In what follows, we first briefly describe relevant field measurements, and then use the proposed framework to infer the aperture distribution in the sub-horizontal fracture and predict production temperature during the thermal test.

4.1 Tracer and thermal data at the AFL testbed

Both the tracer and thermal tests were performed through an injection well and a production well connected by the sub-horizontal fracture. The distance between the injection and production wells was approximately 14.1 m. To perform tracer tests, water was continuously circulated between the injection and production wells at a constant volumetric flow rate of 5.82 L/min. A salt of Cesium-Iodide (CsI) was used as a combined sorptive/conservative tracer, with the cesium cation as a sorptive tracer and the iodine anion as a conservative tracer. The field

results of the multi-component tracer tests are shown in Fig. 11(a). The arrival times of peak concentration are almost identical for the iodine and cesium ions, but the normalized peak magnitude is smaller for cesium. As discussed in Hawkins et al. (2018), this apparent deviation from an equilibrium model results from rate-limited adsorption. The second peaks at approximately 40 min were mainly caused by the continuous reinjection of produced fluids during the tracer tests (Hawkins et al., 2020). To determine the adsorption reaction parameters of cesium ions, Hawkins et al. (2018) performed two batch reactor experiments in which cesium ions dissolved in water were adsorbed onto two rock samples collected at roughly 17 m below the testbed surface. The measured partition coefficients (P_f) are 7.8 and 16.6 cm, and the first-order adsorption rates are 0.4 and 1.33 d^{-1}. In addition to the tracer tests, a pressure test conducted in 2012 recorded a pressure loss of 433 Pa between the injection and production wells under an injection volumetric flow rate of 4.2 L/min. In subsequent ES-MDA analysis, we assume a linear relationship between injection rate and pressure loss, and therefore the pressure loss during the tracer test with a volumetric flow rate of 5.82 L/min can be calculated as 600 Pa.

The thermal test was performed by continuously injecting heated water (74 °C) into the fracture at a constant volumetric flow rate of 5.7 L/min for six days. The measured temperature response at the production well indicated an extremely rapid thermal breakthrough (Fig. 11(b)). After six days, the production well fluid temperature increased approximately 17.7 °C from the initial value of 11.7 °C to a final value of 29.4 °C.

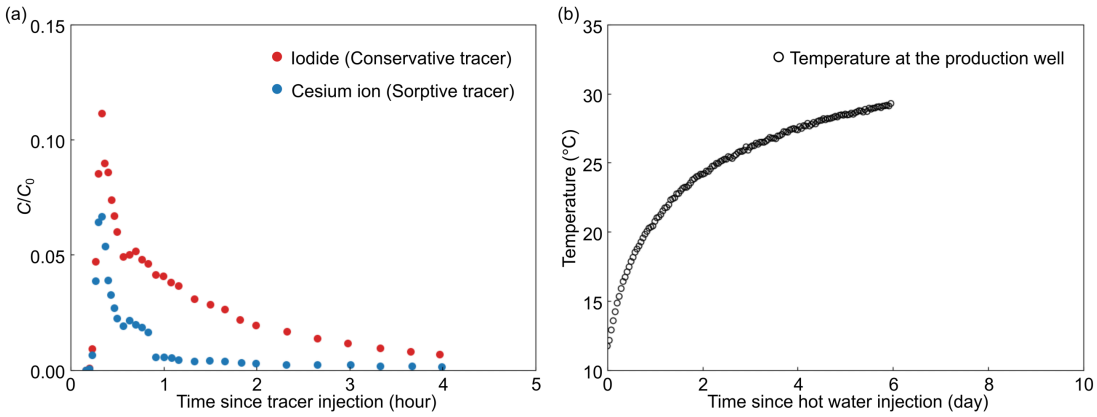

Fig. 11 Results of the tracer and thermal tests at the Altona Field Laboratory testbed. (a) Tracer breakthrough curves at the production well for iodine and cesium ions. The monitored tracer concentration is normalized by injection concentration C_0. (b) Thermal breakthrough curve at the production well during the thermal test.

4.2 Numerical model for tracer and thermal simulation

We develop a 200 × 200 × 20 m^3 model to simulate the tracer and thermal processes in the AFL testbed (Fig. 12). A 32 × 32 m^2 horizontal fracture is assumed 7.6 m below the top surface of the model. The fracture is represented by a 4 mm layer with an in-plane mesh resolution of 0.2 m × 0.2 m. The mesh resolution of the rock is 0.2 m × 0.2 m × 0.5 m near the fracture and gradually increases to 10 m × 10 m × 2 m in the far field. The total element number in the model is approximately 840,000. Based on prior knowledge from Ground Penetrating Radar (GPR) surveys (Hawkins et al., 2018), we assume an oriented aperture distribution from the injection well towards the production well (Fig. 12(b)). Similar to the field-scale EGS model

in Section 3, we generate 5,000 oriented 160 × 160 log-normal random fields and use PCA to represent the aperture field with a 200-dimensional latent space. The first 200 principal components can preserve approximately 62.7% of the total variance in original aperture fields.

For tracer modeling, we only consider the 2D fracture as the porosity and permeability of the surrounding Potsdam Sandstone are negligible relative to the target fracture (Table 2). The fracture boundaries are assumed impermeable. The reinjection of produced fluid is accounted for by specifying tracer injection concentration according to the simulated tracer concentration at the production well. We consider rate-limited adsorption process for the tracer modeling of cesium ion, with the first-order adsorption rate and partition coefficient estimated from the measurements mentioned in Section 4.2 (Table 2). Note that we use a relatively large partition coefficient within the measured range (7.8 – 16.6 cm). For thermal modeling, we consider the whole computational domain in Fig. 12. The upper, lower and lateral model boundaries are assumed impermeable to both fluid and heat. Key parameters for tracer and thermal modeling are obtained from the literature (Hawkins et al., 2017a, 2020), as summarized in Table 2.

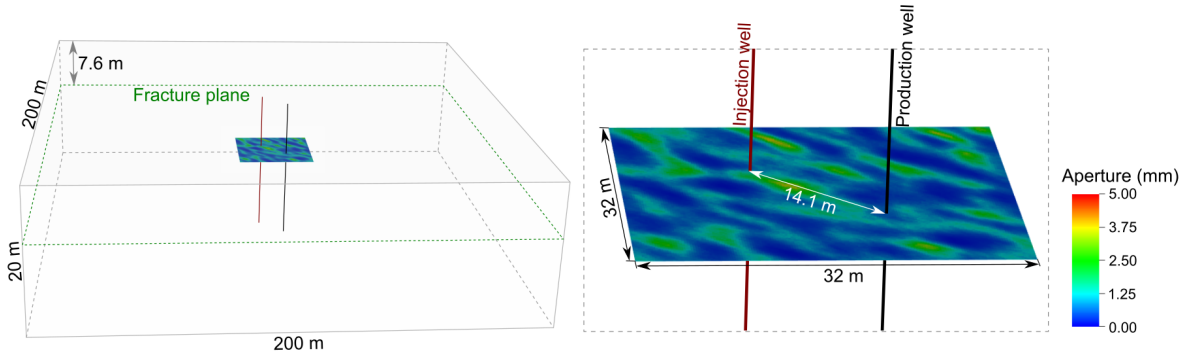

Fig. 12 Three-dimensional model for the Altona Field Laboratory testbed. Note that the scales in the horizontal and vertical directions are different.

Table 2 Parameters for tracer and thermal modeling in the AFL testbed.

Parameter	Value
Porosity of rock	0.01
Permeability of rock (m^2)	1×10^{-16}
Density of rock (kg/m^3)	2500
Specific heat capacity of rock (J/kg/K)	1000
Thermal conductivity of rock (W/m/K)	7.6
Initial temperature in the testbed (°C)	11.7
Density of water (kg/m^3)	1000
Dynamic viscosity of water (Pa·s)	0.001
Compressibility of water (Pa^{-1})	5×10^{-10}
Specific heat capacity of water (J/kg/K)	4200

Longitudinal dispersivity (m)	0.1
Transverse dispersivity (m)	0.01
First-order adsorption rate of cesium ion (d^{-1})	0.865
Partition coefficient of cesium ion (cm)	15.0

4.3 Numerical model for tracer and thermal simulation

The conservative tracer, sorptive tracer and pressure loss data are assimilated simultaneously using ES-MDA. The total number of data points is 66 ($N_d = 66$). The standard deviations are assumed to be 0.003, 0.0024 and 6.5 Pa for the conservative tracer, sorptive tracer and pressure data respectively. The total data assimilation number is 15 ($N_a = 15$), and the ensemble size is 432 ($N_e = 432$).

The measured tracer breakthrough curves for iodine and cesium ions are appropriately reproduced with the obtained posterior ensemble as shown in Fig. 13(a). The pressure loss between the injection and production wells simulated by the posterior ensemble is also consistent with the field measurements (Fig. 13(b)).

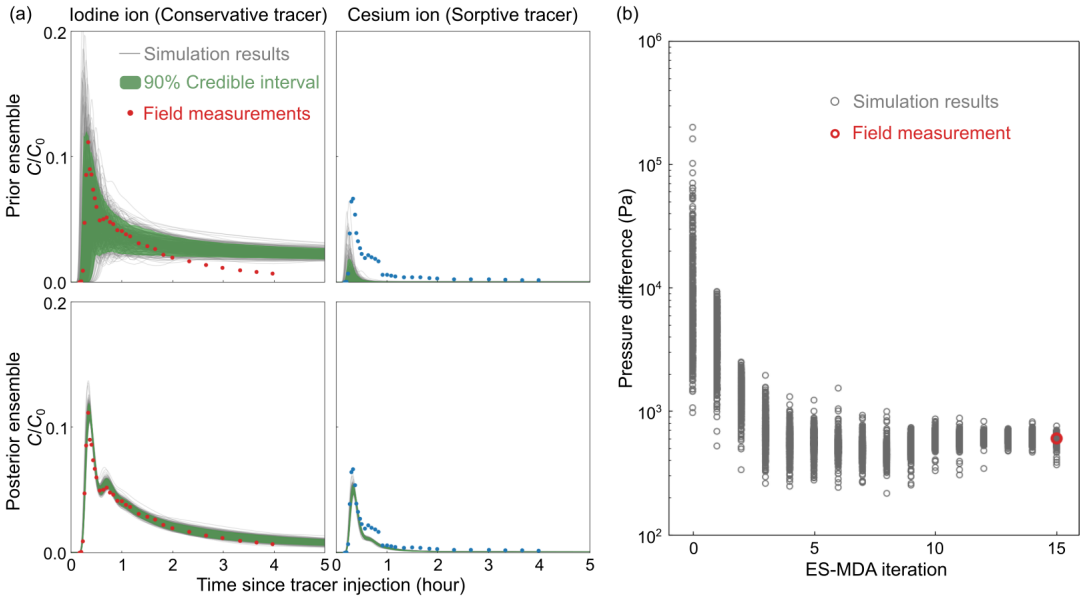

Fig. 13 Simulation results of tracer breakthrough curve and pressure loss at the AFL testbed. (a) Comparison between the simulated (grey curves) and true tracer breakthrough curves (dots) from prior and posterior ensembles. (b) Change of the simulated pressure loss with ES-MDA iterations. Simulation results are shown by grey circles, and the true value is annotated by the red circle.

4.4 Analysis of aperture distribution and fracture flow characteristics

Fig. 14 compares the aperture distribution and flow field calculated from prior and posterior ensembles. Similar to the results of the previous field scale EGS model, the average fracture aperture distribution obtained from prior ensemble is quite uniform, and no remarkable flow channel is observed in the average flow field (Fig. 14(a)). After ES-MDA updates, the average

aperture and flow field from posterior ensemble reveal a narrow flow channel connecting the injection and production wells (Fig. 14(b)). This striking feature is essential for the fit of the tracer breakthrough curve of the sorptive cesium ion. For prior realizations, since the flow field between the injection and production wells is relatively uniform, the effective interaction area (i.e., the fracture-fluid interfacial surface area or "flow-wetted" surface area) between fluid and surrounding rocks is relatively large. As a result, a large portion of the injected cesium ions are adsorbed by the rock and the simulated tracer concentrations at the production well are smaller than the measurements (Fig. 13(a)). For posterior realizations, since most of the fluid is constrained in the narrow flow channel, the fluid-rock interaction area is dramatically reduced, and therefore the simulated tracer breakthrough curves of cesium ion can appropriately match the measurements. Such a narrow flow channel is also consistent with previous GPR surveys (Hawkins et al., 2018).

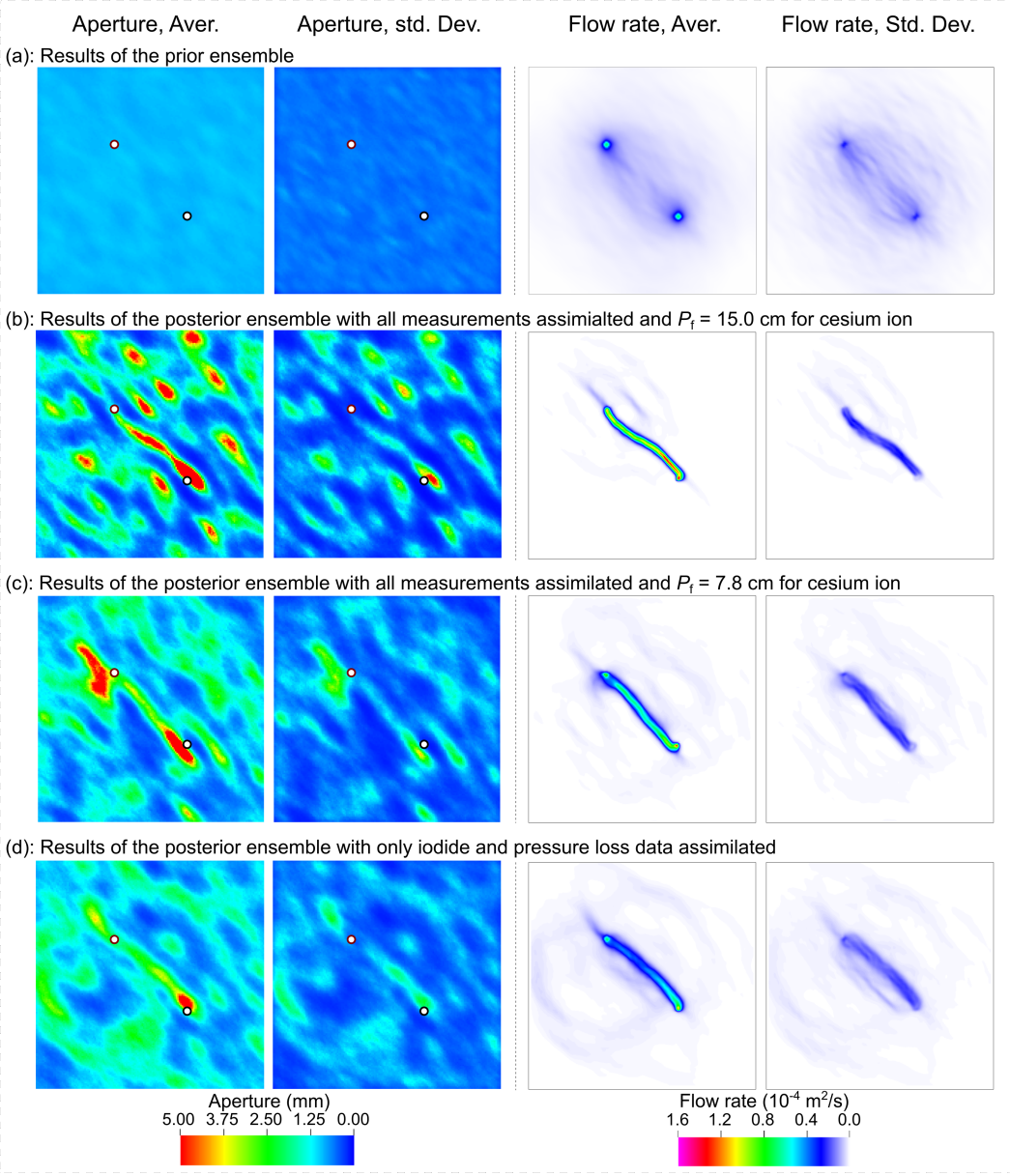

Fig. 14 Average (Aver.) and standard deviation (Std. Dev.) of aperture distribution and flow rate calculated from prior and posterior ensembles. (a) Results for the prior ensemble. (b) Results for

602 the posterior ensemble of the baseline ESMDA which assimilates all measurements
603 simultaneously and uses a relatively large partition coefficient (15.0 cm) for cesium ions. (c)
604 Results for the posterior ensemble of the ESMDA which assimilates all measurements
605 simultaneously and uses a relatively small partition coefficient (7.8 cm) for cesium ions. (d)
606 Results for the posterior ensemble of the ESMDA which only assimilates iodine tracer and
607 pressure loss data.

608 We use a relatively large partition coefficient (15.0 cm) for cesium ions in the above ES-
609 MDA. However, as mentioned previously, the measured partition coefficients from two batch
610 reactor experiments are 7.8 and 16.6 cm, indicating that there exists uncertainty in the
611 appropriate value of the partition coefficient. To examine the impact of an uncertain partition
612 coefficient, we perform a second ES-MDA using a relatively small partition coefficient (7.8 cm)
613 for cesium ions. The obtained posterior ensemble can also match the tracer and pressure
614 measurements, and Fig. 14(c) shows the corresponding average aperture distribution and flow
615 rate in the fracture. The flow field is more diffuse than that in Fig. 14(b). Besides a major flow
616 channel similar to that in Fig. 14(b), several minor flow channels connecting the injection and
617 production wells appear. These minor flow channels enlarge the interaction area between fluid
618 and rock so that the tracer measurements of cesium ion can be matched with a relatively small
619 partition coefficient. We also perform a third ES-MDA that only assimilates the iodine tracer and
620 pressure loss data. The calculated average flow field shows a further scattered flow pattern
621 between the injection and production wells (Fig. 14(d)). The comparison in Fig. 14 indicates that
622 the partition coefficient has significant impacts on fracture flow characterization.

623 4.5 Analysis of temperature response at the production well

624 With the obtained prior and posterior ensembles, we now simulate the water injection test
625 and predict the temperature response at the production well. For each ensemble in Fig. 14, we
626 randomly select 30 realizations to perform thermal modeling. The predicted temperature rise from
627 the prior ensemble is much lower than the measured production temperature, and the results from
628 different realizations show a significant uncertainty (Fig. 15(a)). This is because randomly
629 generated aperture distributions in the prior ensemble result in diffuse flow patterns between the
630 injection and production wells (Fig. 14(a)). Fluid-rock interaction area is relatively large, retarding
631 the temperature increase at the production well. The predicted temperature increase at the end of
632 the hot water injection test varies between 0.0 to 6.0 °C among the 30 realizations (Fig. 15(a)),
633 which are much smaller than the measured temperature increase (17.7 °C) in the field.

634 For the posterior ensemble in Fig. 14(b), the interaction area between fluid and rocks is
635 largely constrained within the narrow flow channel, and therefore the predicted temperature at the
636 production well increases rapidly and agrees well with the measurements (Fig. 15(b)). The
637 predicted temperature increase after six days hot water injection (17.3 to 19.8 °C) is close to the
638 measured temperature increase. For the posterior ensemble in Fig. 14(c), the fluid-rock interaction
639 area is larger than that in Fig. 14(b) because of the minor flow channels. Therefore, the predicted
640 production temperature is smaller than that predicted by the posterior ensemble in Fig. 14(b), and
641 cannot match the measured production temperature (Fig. 15(c)). For the posterior ensemble in Fig.
642 14(d), the fluid-rock interaction area is further enlarged, and the corresponding temperature
643 increase at the production is further reduced (Fig. 15(d)). However, it is worth mentioning that
644 although the temperature predictions in Fig. 15(c) and (d) fail to match the field measurements,
645 they are still better than the predictions from the prior ensemble. Conservative tracer data and

pressure data provide useful information for aperture inference and thermal prediction, but sorptive tracer data is indispensable to correctly predict temperature response. Hawkins et al. (2020) also analyzed the tracer and thermal tests in the AFL testbed. They employed a genetic algorithm (GA) to infer the aperture distribution using a conservative tracer (C-Dot) and pressure data, and then predicted the production temperature. Their results also revealed a narrow flow channel of roughly 1.5 m width between the injection and production wells, but the predicted production temperatures were smaller than field measurements. Incorporating sorptive tracer data in GA might be able to improve the prediction of production temperature.

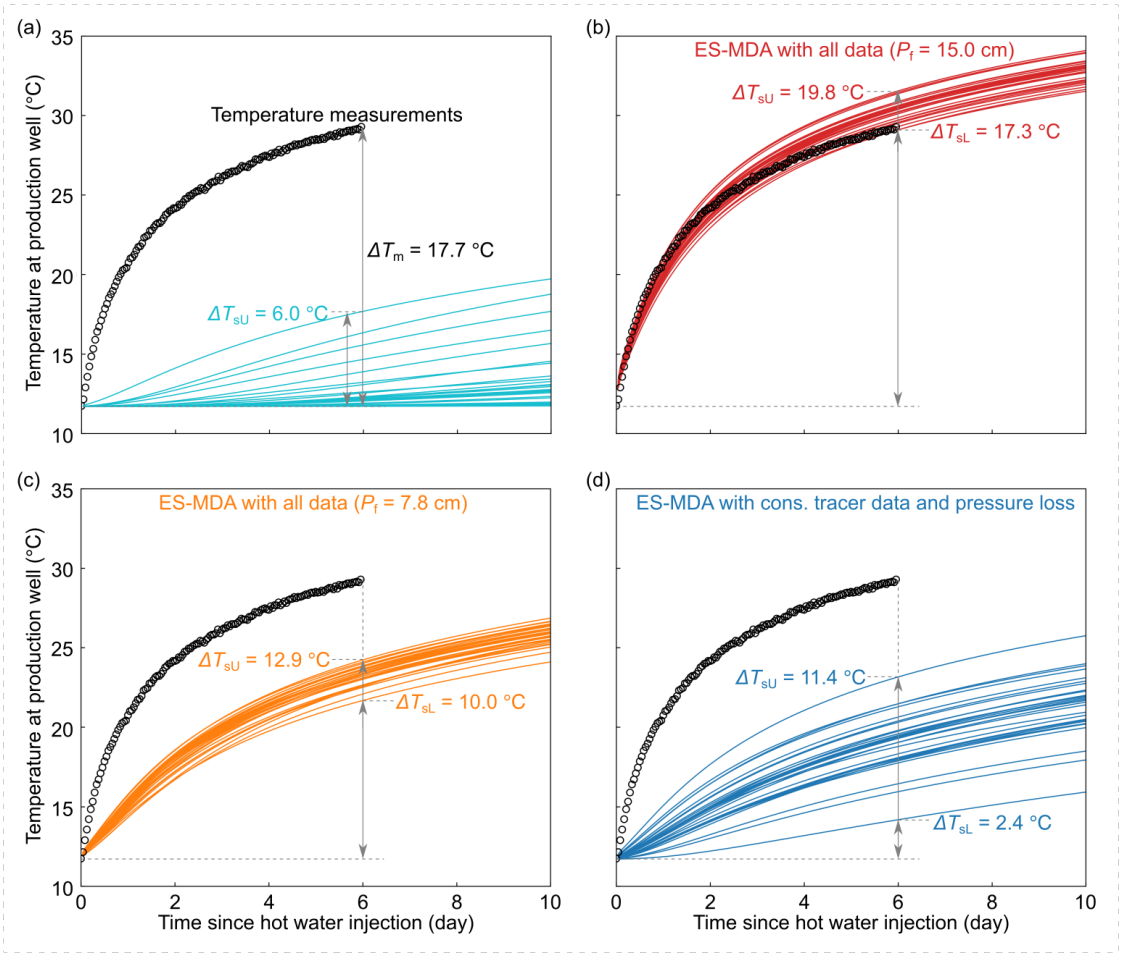

Fig. 15 Predicted and measured temperature responses at the production well during the hot water injection test at the AFL testbed. Temperature increases at the end of the test are annotated. ΔT_m denotes the measured temperate increase, and ΔT_{sU} and ΔT_{sL} are upper and lower bounds of the predicted temperature increase. Results predicted by different ensembles are shown: (a) Prior ensemble. (b) ~ (d) Posterior ensembles obtained by assimilating different data and using different partition coefficients (P_f). The four sub-figures are corresponding to the four rows in Fig. 14.

5 Discussions

5.1 Gaussian and non-Gaussian parameter fields

An important premise of the proposed framework is that model parameters follow a Gaussian or log-normal distribution. On the one hand, PCA is only applicable to random fields that can be fully characterized by two-point statistics (Liu and Durlofsky, 2020), such as the Gaussian fields used in the present study. On the other hand, ES-MDA requires a Gaussian parameter distribution, otherwise its performance could be severely degraded (Canchumuni et al., 2020; Zhang et al., 2020). As mentioned in Section 2.1, latent parameters from PCA follow the standard normal distribution, which perfectly meet the Gaussian requirement of ES-MDA.

Although a Gaussian parameter field (aperture or permeability) is a reasonable assumption for many subsurface reservoirs, a non-Gaussian parameter field, such as a binary/ternary facies field, has been widely adopted to account for highly channelized reservoirs (Lochbühler et al., 2014; Hakim-Elahi and Jafarpour, 2017; Tang et al., 2020). Directly applying the proposed framework to invert for such multi-facies fields inevitably leads to inaccurate inversion results since the proposed framework always assumes a Gaussian (or log-normal) parameter field to enable the use of PCA for dimensionality reduction.

However, an important finding from the present study is that a Gaussian field is able to reproduce highly channelized flow patterns from a non-Gaussian field, and thus provide accurate predictions of reservoir performance. Although the inferred aperture/permeability field might be inaccurate, the underlying flow patterns can be appropriately resolved by matching tracer measurements. For the example in Fig. 2, the "true" aperture field is highly channelized and does not follow a Gaussian or log-normal distribution. It is not even within the Gaussian parameter space that we construct for subsequent ES-MDA. Nevertheless, the flow fields simulated based on the inferred Gaussian aperture fields closely resemble the true flow field (Fig. 7). This is not surprising because tracer recovery is more directly affected by the flow field than by the aperture field. As a result, the thermal performance is accurately predicted (Figs. 6 and 8).

Another solution to address the issue of non-Gaussian parameter field is developing effective parameterization methods that can map high-dimensional non-Gaussian fields to low-dimensional latent parameters that follow Gaussian distributions. In fact, the parameterization of complex geological structures such as binary/ternary facies fields is currently an active research area. Various methods have been proposed, including optimization-based PCA (O-PCA) (Vo and Durlofsky, 2014), discrete cosine transform (Jafarpour and McLaughlin, 2007), and deep learning algorithms such as CNN-PCA (Liu and Durlofsky, 2020), variational autoencoder (VAE) (Laloy et al., 2017; Canchumuni et al., 2019; Mo et al., 2020), and generative adversarial network (GAN) (Laloy et al., 2018; Canchumuni et al., 2020). These parameterization methods have been successfully used for the inference of non-Gaussian permeability fields through ensemble-based data assimilation methods (Canchumuni et al., 2019, 2020; Bao et al., 2020).

5.2 Discrete fracture network (DFN)

Both the synthetic and field cases in the present study have a predominant fracture in the reservoir. However, for many naturally fractured reservoirs, fluid flow may involve multiple interconnected fractures that form a discrete fracture network (DFN). For such reservoirs, the fracture flow patterns depend not only on the aperture distributions of individual fractures but also the geometry of DFN. Extending the proposed framework from a single fracture to DFNs

requires an effective parameterization method that can represent salient information in DFNs relevant to fluid flow with appropriately compromised model complexities.

Current approaches for DFN parameterization usually represent each single fracture by parameters describing its location, orientation, size and aperture to allow individual tuning of fractures (Dorn et al., 2013; Somogyvári et al., 2017; Ma et al., 2020). Such a parameterization induces an extremely high-dimensional parameter space. Moreover, since the number of fractures is not known *a priori*, the dimensionality may vary in the inversion process, making most inversion/data assimilation methods inapplicable, including the proposed framework. A possible solution to this difficulty is using advanced deep learning algorithms (such as VAE and GAN) to generate high-fidelity DFN models from low-dimensional latent spaces. The capability of GAN and VAE in reproducing complex data structures and preserving data statistics has been widely reported. Their application in parameterizing DFNs with highly discontinuous structures deserves further investigations.

5.3 Implications for subsurface characterization and analysis

Although tracer testing has been widely used for subsurface characterization, how to effectively interpret tracer data and whether the interpretation results (permeability or aperture distribution) can correctly predict long-term performance has not been adequately elucidated previously. The present study attempts to answer these questions and provides a new framework for the characterization and analysis of fractured reservoirs. The analyses of a synthetic EGS model and a field geothermal test indicate that tracer data contain essential information regarding subsurface flow characteristics. The proposed framework is able to retrieve necessary flow information to accurately predict thermal performance in the two examples considered here. Moreover, because the framework uses an ensemble-based data assimilation method, uncertainties arising from biased prior knowledge and measurement errors can be naturally tackled. We demonstrate how these uncertainties propagate to the inverted aperture distribution and fracture flow pattern, and further to the thermal prediction in the two cases.

An important implication for real-world applications is that both conservative and sorptive tracer tests need to be conducted to sufficiently characterize subsurface fractures for thermal prediction. Both the synthetic and field cases in the present study indicate that conservative tracers alone are unable to constrain fracture aperture, leading to biased predictions with large uncertainties. In several previous attempts to predict thermal performance from tracer data (Vogt et al., 2012b; Hawkins et al., 2020; Wu et al., 2021), the predicted thermal performance either indicates significant uncertainty or cannot qualitatively match field measurements. A possible reason is that only conservative tracer data was used for aperture/permeability inversion in these attempts. In addition, when sorptive tracer data is available, the sorption parameters such as partition coefficient need to be carefully measured. The field case clearly shows the remarkable impact of partition coefficient on aperture inversion and thermal prediction (Figs. 14 and 15).

7 Conclusions

We proposed a tracer data interpretation framework to predict the long-term thermal performance of EGS from tracer tests. The framework first inverts for the spatial distribution of fracture aperture through an ensemble-based data assimilation method, and then uses the inversion results to predict thermal performance. A synthetic case with a field-scale EGS model

and a real-world case involving meso-scale tracers and thermal tests were analyzed to demonstrate the capability of the framework. For both cases, thermal performance was accurately predicted and the associated uncertainty was appropriately quantified through the obtained posterior model ensembles. By interpreting practically available tracer, pressure and flow data, the framework can provide informative guidance for reservoir optimization and long-term risk management.

The correct prediction of thermal performance requires the joint assimilation of conservative and sorptive tracer data. Sorptive tracer data is indispensable to properly characterize fracture flow patterns, especially the effective fluid-rock interaction area which is critical for thermal prediction. Analysis without of sorptive tracer data tends to overestimate fluid-rock interaction, leading to biased prediction of thermal performance with relatively large uncertainties.

Besides tracer, pressure and flow data, other types of data such as deformation and seismic data can also be interpreted using the proposed framework. Since physical models for deformation and seismic modeling are different from that for tracer transport, we need to replace the forward simulation in the framework accordingly. Of course, the predictive ability of the interpretation results highly depends on the relationship between the data being interpreted and the quantity to be predicted. For the EGS examples in the present study, the strong connection between tracer transport and heat extraction processes is the basis for predicting thermal performance from tracer data.

Acknowledgments, Samples, and Data

This research was performed in support of the EGS Collab project; taking place in part at the Sanford Underground Research Facility in Lead, South Dakota. The assistance of the Sanford Underground Research Facility and its personnel in providing physical access and general logistical and technical support is acknowledged. Support from the EGS Collab team is gratefully acknowledged. This work was supported by U.S. Department of Energy, Geothermal Technologies Office, and performed under the auspices of the U.S. Department of Energy by Lawrence Livermore National Laboratory under Contract DE-AC52-M07NA27344. The field data at the Altona Field Laboratory (AFL) can be found in previously published papers as cited. This document is LLNL report LLNL-JRNL-823464.

References

Ayling, B. F., Hogarth, R. A., Rose, P. E. (2016). Tracer testing at the Habanero EGS site, central Australia. *Geothermics*, *63*, 15-26.

Bao, J., Li, L., Redoloza, F. (2020). Coupling ensemble smoother and deep learning with generative adversarial networks to deal with non-Gaussianity in flow and transport data assimilation. *Journal of Hydrology*, *590*, 125443.

Berkowitz, B. (2002). Characterizing flow and transport in fractured geological media: A review. *Advances in Water Resources*, *25*, 861-884.

Brown, D. W., Duchane, D. V., Heiken, G., Hriscu, V. T. (2012). Mining the Earth's Heat: Hot Dry Rock Geothermal Energy. Springer, Berlin.

Canchumuni, S. W. A., Castro, J. D. B., Potratz, J., Emerick, A. A., Pacheco, M. A. C. (2020). Recent developments combining ensemble smoother and deep generative networks for facies history matching. *Computational Geosciences*, *25*, 433-466.

Canchumuni, S. W. A., Emerick, A. A., Pacheco, M. A. C. (2019). Towards a robust parameterization for conditioning facies models using deep variational autoencoders and ensemble smoother. *Computers and Geosciences*, *128*, 87-102.

Chen, X., Hammond, G. E., Murray, C. J., Rockhold, M. L., Vermeul, V. R., Zachara, J. M. (2013). Application of ensemble-based data assimilation techniques for aquifer characterization using tracer data at Hanford 300 area. *Water Resources Research*, *49*(10), 7064-7076.

Chen, Y., Oliver, D. S. (2012). Ensemble randomized maximum likelihood method as an iterative ensemble smoother. *Mathematical Geosciences*, *44*, 1-26.

Chen, Y., Zhao, Z. (2020). Heat transfer in a 3D rough rock fracture with heterogeneous apertures. *International Journal of Rock Mechanics and Mining Sciences*, *134*, 104445.

Crestani, E., Camporese, M., Baú, D., Salandin, P. (2013). Ensemble Kalman filter versus ensemble smoother for assessing hydraulic conductivity via tracer test data assimilation. *Hydrology and Earth System Sciences*, *17*(4), 1517-1531.

Cui, T., Fox, C., O'Sullivan, M. J. (2011). Bayesian calibration of a large-scale geothermal reservoir model by a new adaptive delayed acceptance Metropolis Hastings algorithm. *Water Resources Research*, *47*, W10521.

Dorn, C., Linde, N., Borgne, T. L., Bour, O., de Dreuzy J. R. (2013). Conditioning of stochastic 3-D fracture networks to hydrological and geophysical data. *Advances in Water Resources*, *62*, 79-89.

Emerick, A. A., Reynolds, A. C. (2013). Ensemble smoother with multiple data assimilation. *Computers and Geosciences*, *55*, 3-15.

Evensen, G. (1994). Sequential data assimilation with a nonlinear quasi-geostrophic model using Monte Carlo methods to forecast error statistics. *Journal of Geophysical Research*, *99*, 10143-10162.

Evensen, G. (2018). Analysis of iterative ensemble smoothers for solving inverse problems. *Computational Geosciences*, *22*, 885-908.

Fienen, M. N., Luo, J., Kitanidis, P. K. (2006). A Bayesian geostatistical transfer function approach to tracer test analysis. *Water Resources Research*, *42*, W07426.

Fox, D. B., Koch, D. L., Tester, J. W. (2015). The effect of spatial aperture variations on the thermal performance of discretely fractured geothermal reservoirs. *Geothermal Energy*, *3*(1), 1-29.

Fu, P., Hao, Y., Walsh, S. D. C., Carrigan, C. R. (2016). Thermal drawdown-induced flow channeling in fractured geothermal reservoirs. *Rock Mechanics and Rock Engineering*, *49*(3), 1001-1024.

Guo, B., Fu, P., Hao, Y., Carrigan, C. R. (2016a). Investigating the possibility of using tracer tests for early identification of EGS reservoirs prone to flow channeling. 41st Workshop on Geothermal Reservoir Engineering, Stanford, CA.

Guo, B., Fu, P., Hao, Y., Peters, C. A., Carrigan, C. R. (2016b). Thermal drawdown-induced flow channeling in a single fracture in EGS. *Geothermics*, *61*, 46-62.

Hakim-Elahi, S., Jafarpour, B. (2017). A distance transform for continuous parameterization of discrete geologic facies for subsurface flow model calibration. *Water Resources Research*, *53*, 8226-8249.

Hawkins, A. J., Becker, M. W., Tester, J. W. (2018). Inert and adsorptive tracer tests for Field measurement of flow-wetted surface area. *Water Resources Research*, *54*, 5341-5358.

836 Hawkins, A. J., Fox, D. B., Matthew, M. W., Tester, J. W. (2017a). Measurement and simulation
837 of heat exchange in fractured bedrock using inert and thermally degrading tracers. *Water*
838 *Resources Research*, *53*, 1210-1230.
839 Hawkins, A. J., Becker, M. W., Tsoflias, G. P. (2017b) Evaluation of inert tracers in a bedrock
840 fracture using ground penetrating radar and thermal sensors. *Geothermics*, *67*, 86-94.
841 Hawkins, A. J., Fox, D. B., Koch, D. L., Becker, M. W., Tester, J. W. (2020). Predictive inverse
842 model for advective heat transfer in a short-circuited fracture: Dimensional analysis,
843 machine learning, and field demonstration. *Water Resources Research*,
844 *56*, e2020WR027065.
845 Hawkins, A. J., Bender, J. T., Grooms, R. D., Schissel, C. J., Tester, J. W. (2021). Temperature-
846 responsive smart tracers for field-measurement of inter-well thermal evolution:
847 Heterogeneous kinetics and field demonstration. *Geothermics*, *92*, 102046.
848 Irving, J., Singha, K. (2010). Stochastic inversion of tracer test and electrical geophysical data to
849 estimate hydraulic conductivities. *Water Resources Research*, *46*(11), W11514.
850 Jafarpour, B., McLaughlin, D. B. (2007). Efficient permeability parameterization with the
851 discrete cosine transform. SPE reservoir simulation symposium, Houston, Texas, USA.
852 Juliusson, E., Horne, R. N. (2013). Characterization of fractured reservoirs using tracer and flow-
853 rate data. *Water Resources Research*, *49*, 2327-2342.
854 Keller, J., Hendricks Franssen, H. J., Marquart, G. (2018). Comparing seven variants of the
855 ensemble Kalman filter: How many synthetic experiments are needed? *Water Resources*
856 *Research*, *54*, 6299-6318.
857 Kittilä, A., Jalali, M. R., Evans, K. F., Willmann, M., Saar, M. O., Kong, X. Z. (2019). Field
858 comparison of DNA-labeled nanoparticle and solute tracer transport in a fractured
859 crystalline rock. *Water Resources Research*, *55*(*8*), 6577-6595.
860 Laloy, E., Hérault, R., Jacques, D., Linde, N. (2018). Training-image based geostatistical
861 inversion using a spatial generative adversarial neural network. *Water Resources*
862 *Research*, *54*(1), 381-406.
863 Laloy, E., Hérault, R., Lee, J., Jacques, D., Linde, N. (2017). Inversion using a new low-
864 dimensional representation of complex binary geological media based on a deep neural
865 network. *Advances in Water Resources*, *110*, 387-405.
866 Liu, Y., Durlofsky, L. J. (2020). 3D CNN-PCA: A deep-learning-based parameterization for
867 complex geomodels. *Computers and Geosciences*, *148*, 104676.
868 Lochbühler, T., Pirot, G., Straubhaar, J., Linde, N. (2014). Conditioning of multiple-point
869 statistics facies simulations to tomographic images. *Mathematical Geosciences*, *46*, 625-
870 645.
871 Ma, X., Zhang, K., Yao, C., Zhang, L., Wang, J., Yang, Y., Yao, J. (2020). Multiscale-network
872 structure inversion of fractured media based on a hierarchical-parameterization and data-
873 driven evolutionary-optimization Method. *SPE Journal*, *25*(*5*), 2729-2748.
874 Maxwell, S. C., Rutledge, J., Jones, R., Fehler, M. (2010). Petroleum reservoir characterization
875 using downhole microseismic monitoring. *Geophysics*, *75(5)*, 75A129-75A137.
876 Mo, S., Zabaras, N., Shi, X., Wu, J. (2020). Integration of adversarial autoencoders with residual
877 dense convolutional networks for estimation of non-Gaussian hydraulic conductivities.
878 *Water Resources Research*, *56*(2), e2019WR026082..
879 Neuman, S. P. (2005). Trends, prospects and challenges in quantifying flow and transport
880 through fractured rocks. *Hydrogeology Journal*, *13*(1), 124-147.

Power, W. L., Tullis, T. E. (1992). The contact between opposing fault surfaces at Dixie Valley, Nevada, and implications for fault mechanics. *Journal of Geophysical Research*, *97*, 15425-15435.

Pyrak-Nolte, L. J., Morris, J. P. (2000). Single fractures under normal stress: The relation between fracture specific stiffness and fluid flow. *International Journal of Rock Mechanics and Mining Sciences*, *37*, 245-262.

Radilla, G., Sausse, J., Sanjuan, B. & Fourar, M. (2012). Interpreting tracer tests in the enhanced geothermal system (EGS) of Soultz-sous-Forêts using the equivalent stratified medium approach. *Geothermics*, *44*, 43-51.

Sanjuan, B., Pinault, J. L., Rose, P., Gérard, A., Brach, M., Braibant, G., Crouzet, C., Foucher, J. C., Gautier, A., Touzelet, S. (2006). Tracer testing of the geothermal heat exchanger at Soultz-sous-Forêts (France) between 2000 and 2005. *Geothermics*, *35*, 622-653.

Sarma, P., Durlofsky, L. J., Aziz, K. (2008). Kernel principal component analysis for efficient differentiable parameterization of multipoint geostatistics. *Mathematical Geosciences*, *40*, 3-32.

Settgast, R. R., Fu, P., Walsh, S. D. C., White, J. A., Annavarapu, C., Ryerson, F. J. (2017). A fully coupled method for massively parallel simulation of hydraulically driven fractures in 3-dimensions. *International Journal for Numerical and Analytical Methods in Geomechanics*, *41*, 627-653.

Shook, G. M. (2001). Predicting thermal breakthrough in heterogeneous media from tracer tests. *Geothermics*, *30*, 573-589.

Shook, G.M. (2003). A simple, fast method of estimating fractured geometry from tracer tests. *Geothermal Resources Council Transactions*, *27*, 407-411.

Shook, G. M., Suzuki, A. (2017). Use of tracers and temperature to estimate fracture surface area for EGS reservoirs. *Geothermics*, *67*, 40-47.

Somogyvári, Y., Jalali, M., Jimenez Parras, S., Bayer, P. (2017). Synthetic fracture network characterization with transdimensional inversion. *Water Resources Research*, *53*(*6*), 5104-5123.

Suzuki, A., Ikhwanda, F., Yamaguchi, A., Hashida, T. (2019). Estimations of fracture surface area using tracer and temperature data in geothermal fields. *Geosciences*, *9*, 425.

Tang, H., Fu, P., Sherman, C. S., Zhang, J., Ju, X., Hamon, F., Azzolina, N. A., Burton-Kelly, M., Morris, J. P. (2021). A deep learning-accelerated data assimilation and forecasting workflow for commercial-scale geologic carbon storage. arXiv preprint: 2105.09468.

Tang, M., Liu, Y., Durlofsky, L. J. (2019). A deep-learning-based surrogate model for data assimilation in dynamic subsurface flow problems. *Journal of Computational Physics*, *413*, 109456.

Tian, W., Wu, X., Shen, T., Kalra, S. (2016). Estimation of hydraulic fracture volume utilizing partitioning chemical tracer in shale gas formation. *Journal of Natural Gas Science and Engineering*, *33*, 1069-1077.

van Leeuwen, P. J., Evensen, G. (1996). Data assimilation and inverse methods in terms of a probabilistic formulation. *Monthly Weather Review*, *124*, 2898-2913.

Vo, H. X., Durlofsky, L. J. (2014). A new differentiable parameterization based on principal component analysis for the low-dimensional representation of complex geological models. *Mathematical Geosciences*, *46*(7), 775-813.

Vogt, C., Kosack, C., Marquart, G. (2012a). Stochastic inversion of the tracer experiment of the enhanced geothermal system demonstration reservoir in Soultz-sous-Forêts — Revealing pathways and estimating permeability distribution. *Geothermics*, *42*, 1-12.

Vogt, C., Marquart, G., Kosack, C., Wolf, A., Clauser, C. (2012b). Estimating the permeability distribution and its uncertainty at the EGS demonstration reservoir Soultz-sous-Forêts using the ensemble Kalman filter. *Water Resources Research*, *4*8, W08517.

Vrugt, J. A. (2016). Markov chain Monte Carlo simulation using the DREAM software package: Theory, concepts, and MATLAB implementation. *Environmental Modelling and Software*, *75*, 273-316.

Wu, H., Fu, P., Morris, J. P., Mattson, E. D., Neupane, G., Smith, M. M., Hawkins, A. J., Zhang, Y., Kneafsey, T., EGS Collab. (2021). Characterization of flow and transport in a fracture network at the EGS Collab field experiment through stochastic modeling of tracer recovery. *Journal of Hydrology*, *593*, 125888.

Wu, H., Fu, P., Morris, J. P. (2020). Predicting thermal responses at the EGS Collab testbed based on tracer test-inferred flow fields. 45th Workshop on Geothermal Reservoir Engineering, Stanford, CA..

Wu, H., Fu, P., Yang, X., Morris, J. P., Johnson, T. C., Settgast, R. R., Ryerson, F. J. (2019). Accurate imaging of hydraulic fractures using templated electrical resistivity tomography. *Geothermics*, *81*, 74-87.

Wu, X., Pope, G. A., Shook, G. M., Srinivasan, S. (2008). Prediction of enthalpy production from fractured geothermal reservoirs using partitioning tracers. *International Journal of Heat and Mass Transfer*, *51*, 1453-1466.

Zhang, J., Man, J., Lin, G., Wu, L., Zeng, L. (2018). Inverse modeling of hydrologic systems with adaptive multifidelity Markov Chain Monte Carlo simulations. *Water Resources Research*, *54*(7), 4867-4886.

Zhang, J., Zheng, Q., Wu, L., Zeng, L. (2020). Using deep learning to improve ensemble smoother: Applications to subsurface characterization. *Water Resources Research*, *56*, e2020WR027399.